Radiophysics and Quantum Electronics, Vol. 57, No. 1, June, 2014
(Russian Original Vol. 57, No. 1, January, 2014)

RECENT TRENDS IN MULTIMODAL OPTICAL COHERENCE TOMOGRAPHY. I. POLARIZATION-SENSITIVE OCT AND CONVENTIONAL APPROACHES TO OCT ELASTOGRAPHY

V. Yu. Zaitsev,[1,2,3] * **V. M. Gelikonov,**[1,2,3]
L. A. Matveev,[1,2] **G. V. Gelikonov,**[1,2]
A. L. Matveyev,[1,2] **P. A. Shilyagin,**[1,2] **and**
I. A. Vitkin,[2,4]

UDC 681.787.7

We discuss physical principles of obtaining polarization-sensitive images, elastographic mapping and visualization of blood circulation/vasculature in optical coherence tomography (OCT). Along with the general overview of the respective methods, we perform comparative critical analysis of some of them from the viewpoint of their feasibility and requirements to OCT systems destined for combining the above-mentioned different image modalities.

1. INTRODUCTION

Since the first successful demonstrations [1-2] of visualizing biological tissue structure by the use of optical coherence tomography (OCT), significant attention in the further studies was focused not only on improvement of resolution and increasing the rate of acquiring conventional structural images, but also on modifications of the very principle of OCT image formation and the development of new methods of OCT image processing aimed at visualization of new types of tissue parameters. Indeed, simultaneous mapping of several functionally different characteristics of biological tissues can significantly increase the information content and correspondingly improve the specificity of diagnostics based on OCT inspection. Such functionally different types of OCT-based visualization include polarization-sensitive images, elastographic images that characterize mechanical properties of tissues (stiffness), and OCT-based mapping of microcirculation of blood in the inspected region (i.e., angiographic imaging). Besides these, one can also combine structural OCT images with images of tissue fluorescence [3], combining multispectral and spectral-domain OCT microscopy [4], performing OCT at significantly different spectral ranges [5–7], and so on.

In contrast to other medical imaging methods, such as ultrasonic or magnetic resonance imaging, for which reproducibility of inspection of the same region by different technical means is not particularly problematic due to relatively large scales of the imaged regions, the OCT techniques deal with much smaller scales on the order of a few millimeters or even less. Consequently, sufficiently exact superposing and comparing of images obtained by different specialized OCT scanners becomes more problematic, which significantly reduces the usefulness of such combined inspection. However, designing multimodal OCT systems combining a large number of different image types necessitates the use of both complex constructions of hardware and the corresponding complications in processing of the scattered optical signals. In view of this, even the possibility of combining only two or three visualization types in a single OCT system (e.g.,

* vyuzai@hydro.appl.sci-nnov.ru

[1] Institute of Applied Physics of the Russian Academy of Sciences; [2] Medical Academy of Nizhny Novgorod; [3] State University of Nizhny Novgorod, Nizhny Novgorod, Russia [4] University of Toronto, Toronto, Canada.
Translated from Izvestiya Vysshikh Uchebnykh Zavedenii, Radiofizika, Vol. 57, No. 1, pp. 59–74, January 2014. Original article submitted October 9, 2013; accepted January 31, 2014.

by analogy with medical ultrasonic scanners supplemented with the elastographic mode) is of significant practical interest and requires complementary solution of rather non-trivial physical and technical problems typical of each of the combined visualization modes.

In the present work, we limit ourselves to the discussion of three OCT visualization types complementing conventional structural (intensity) images. The first part of the paper considers approaches to obtaining improved polarization-sensitive OCT images and the principles of elastographic mapping based on the initial reconstruction of the displacement field in deformed biological tissues. The latter approach is somewhat similar to elastographic methods used in medical ultrasound. In the second part of the paper, we discuss recently proposed OCT-specific methods of elastographic mapping that do not require preliminary reconstruction of the displacement field but rather make use of the correlation stability of compared distorted OCT images, as well as methods for visualization of the blood microcirculation, which in fact are based on rather similar speckle stability principles.

Along with the general overview of respective approaches, we compare and analyze the feasibility of the underlying physical principles central to the above-mentioned visualization methods. We also discuss requirements of the OCT systems from the viewpoint of the possibility of combining such different imaging modalities while minimizing additional construction units that could significantly increase the system hardware and software complexity, as well as its cost.

2. POLARIZATION-SENSITIVE OCT

Polarization-sensitive methods in OCT extend bio-medical visualization by increasing the information value of the OCT inspection via extraction of qualitatively new information about tissue properties. For example, in conventional OCT methods the "regular" (spatially homogeneous) birefringence of tissue manifests itself in the form of modulation of the image brightness as a function of the depth (which is due to the phase delay between the normal optical modes propagating in the medium). In the more general case, the backscattered radiation acquires a cross-polarization component with the polarization orthogonal to that in the incident optical beam. It is known that the appearance of the cross-polarization signal can be related to such factors as regular birefringence, anisotropy of the scattering at the microscopic level (for scatterer sizes smaller than the optical wavelength), the influence of scattering particles shape and the spatial structure of the scattering medium [8]. In endoscopic inspection of soft tissues, polarization-sensitive methods can significantly improve reliability of conclusions on the state of the tissue based on a qualitative consideration of polarization-sensitive images (however, their quantitative interpretation can be significantly complicated in view of strong deformability of surface tissue layers in some organs). By now, a number of methods for polarization-sensitive visualization in OCT has been developed, and the corresponding biomedical experimental studies have begun to reveal the specificity of new information and estimate its diagnostic utility [9]. In most studies, the approach to improve the information value of polarization-sensitive imaging is based on the analysis of the relation between the regular birefringence and variation in the polarization state of the optical signal backscattered from different depths of the inspected tissue region [10–14]. Interferometric selection of the depth, from which the signal is backscattered, and measurement of the variation in its polarization with respect to the incident-wave polarization allow one to determine such properties as depolarization, birefringence, dichroism, and orientation of polarization axes [15, 16]. Such polarization characteristics provide information on the presence of certain ordered structures (e.g., concentration and type of collagen fibers, their local orientation in the near-surface layers [15, 17]), as well as on the tissue microstructural features [15]. The evolution of polarization as a function of the scattering depths is usually characterized using the formalism of Jones and Mueller matrices [11–13, 18–21].

2.1. Cross-polarization images in OCT as a source of additional information from biological tissue

Among various polarization-sensitive methods developed in OCT, an important approach is when the backscattered radiation is analyzed in two orthogonal polarizations produced by different means [16]. The radiation with polarization coinciding with that of the initial signal is received in the so-called co-channel, whereas the signal with the orthogonal polarization is recorded in the cross-channel of the OCT scanner. In the cross-channel the backscattered radiation can appear due to the influence of both regular birefringence and scattering from individual heterogeneities in tissue [6, 8, 17, 22–24]. The degree of backscattering into the orthogonal polarization depends on the size, structure, and anisotropy properties of the optical heterogeneities in the medium [8] and can characterize, for example, the state of collagen tissues, which is especially important for diagnostics of cancer pathologies [17, 25]. As experiments indicate [8], the effectiveness of cross-polarization scattering is especially high for relatively large-scale heterogeneities and is much weaker manifested for heterogeneities with sizes smaller than the optical wave length.

Under conditions of weak birefringence, the cross-polarization scattering can become the main mechanism of the appearance of signals with orthogonal polarization. Obtaining and comparing OCT scans visualizing the distribution of backscattering efficiency into the co-polarization component (the same polarization as in the initial wave) and into cross-polariazation one (with orthogonal polarization) is the basis for one of the polarization-sensitive methods in OCT, referred to as the cross-polarization OCT [6, 8, 17, 22–24]. The first results of application of the cross-polarization OCT [6, 8] showed that the images obtained via the cross-polarization channel (cross-polarization images) significantly differ from those in the co-polarization channel and provide new information about the tissue. For cross-polarization images, the signal from the near-surface layers (where the photons propagate without efficient scattering into the cross polarization) is much weaker than in the co-polarization images. This is favorable for reduction of over-illumination of the near-surface layers and allows for more detailed characterization of structures localized near the tissue boundary. Similarly, for deeper structures that were hardly distinguishable in the co-polarization images, the cross-polarization scans can yield significantly more contrast [6]. Relatively large-scale discrete scattering particles are often better distinguished in the cross-polarization images, and comparison of the latter with co-polarization ones can significantly improve the visualization contrast for certain types of structures in biological tissues [6, 8]. Additional detailed studies are required for determining the composition and morphology of biological structures that appear particularly bright in the cross-polarization OCT [6, 8].

Besides, cross-polarization images give very useful complementary structural information in comparison with co-polarization scans, which makes it possible to detect distortions caused by even a fairly weak regular birefringence. It is known, for example, that the level of the backscattered signal can be significantly reduced exclusively due to polarization effects, when the optical delay between the normal modes in the medium is small and does not exceed half of the wavelength [13, 15, 26].

Such effects can occur in OCT inspection of certain soft biological tissues (e.g., mucous ones and serous coats) with weak birefringence (see Fig. 1). In the right part of the co-polarization image shown in Fig. 1*a*, one can see a significant reduction in the intensity of the signal from deeper regions (the corresponding region is indicated by a dashed line). However, straightforward assignment of this signal reduction to reduced backscattering is incorrect. The cross-polarization image of the same region shown in Fig. 1*b* clearly demonstrates a fairly uniform distribution of the backscattering coefficient in the lateral direction, which indicates that these sub-surface layers have a fairly uniform structure. The observed reduction in the signal visible in the co-polarization channel is evidently due to the influence of a relatively weak tissue birefringence. In the cross-polarization image, the intensity modulation caused by the birefringence is out-of-phase with that in the co-polarization image. This allows one to identify the corresponding artifacts in the co-polarization images and perform the appropriate correction.

It should be noted that an important issue in cross-polarization OCT is a rather complex dependence of the received signals on both polarization of the primary probing wave and orientation of anisotropy axes in the inspected tissue [9]. For example, if the vector of linear polarization of the probing wave occasionally

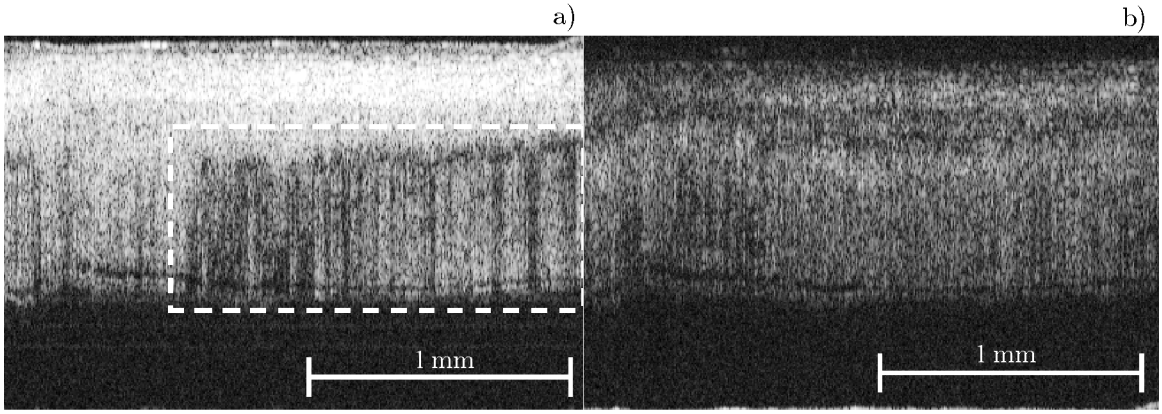

Fig. 1. OCT image of human-eye sclera obtained in the conventional way (*a*) using the co-polarization channel and the complementary cross-polarization image (*b*).

coincides with the axis of the the medium anisotropy, the presence of birefringence does not manifest itself in the obtained OCT image. This phenomenon can be efficiently eliminated by using modulation of the probing-wave polarization [27–29] or utilizing a pair of coherent [30, 31] or incoherent [16, 32] waves with orthogonal polarizations. Further, the signal in the cross-polarization channel depends on the polarization state of the primary probing wave, in contrast with the reception of only the co-polarized wave which is independent of it.

For example, if the linearly polarized wave is backscattered from a structure with random distribution of sizes and shapes of scatterers (e.g. paper), then the intensity of the OCT signal with co-polarization is about 4 dB greater than the intensity of the cross-polarized component [31, 33]. In contrast, for scattering of initially circularly polarized waves under the same conditions, the intensities of co- and cross-components become equal. According to theoretical results and experimental data obtained for Rayleigh scattering, the intensities in the co- and cross-polarized channels also differ by 4 dB [31, 33]. It has been shown [8] that for scattering of linearly polarized light in biological tissues, approximately the same ratio between the two components is observed. However, for scattering from artificial spherical particles embedded into a gel-like matrix, the ratio between the intensities of the co- and cross-polarized components depends on the size and concentration of the inclusions in a complex manner. For sub-wavelength spheres, the difference can be higher and reach 20 dB. We emphasize that this effect is specifically due to scattering at individual inclusions and does not depend on the regular birefringence.

2.2. Methods of obtaining cross-polarization images in OCT

In the design of polarization-sensitive OCT, significant attention is paid to optimization of optical schemes and regimes of their operation in order to obtain the maximum information content and ensure feasibility in clinical practice. Presently, the best information value is reached in cross-polarization optical schemes of OCT based on bulk optical elements [10, 11, 13, 18, 34], as well as for diagnostic optical-fiber systems, in which the inspection does not require flexible variation of the optical paths [35, 36]. In the design of flexible endoscopic OCT systems, the transfer of the above mentioned polarization-sensitive approaches to schemes based on optical fibers is challenging.

At a certain stage of the OCT development, an important role was played by optical-fiber systems based on anisotropic fibers that were able to maintain the interference signal under continuous deformation of the signal arm [6, 37, 38]. Then it was proposed to compensate for the influence of the optical-path deformation on the signal level by applying not only polarization-maintaining anisotropic fibers, but also using the so-called “common path” optical schemes based on isotropic fibers [30, 31, 39–42]. The main feature of such schemes is that both probing (sample) and reference beams propagate along the same path, because

the reference beam is reflected back at the distal end of the optical-fiber probe. Due to this, the common-path schemes ensure reproducibility of flexible fiber-optic probes [31]. It can be noted that in the common-path interferometric optical schemes based on isotropic fibers, the probing-wave polarization can be arbitrary, whereas the optical path difference between the reference and sample waves exceeds the coherence length. In view of this, to single out the interference signal one should use an auxiliary compensating interferemeter. Such an optical scheme [40, 43] included a fiber-optic variant of the Fizeau interferometer which plays the role of a common optical part for the signal and reference waves [44], as well as an autocorrelator based on a Michelson interferometer with Faraday mirrors [45]. The first applications of $\pi/4$ Faraday cells for compensation for phase anisotropy in single-mode fibers were reported in [46, 47].

The usefulness of polarization-sensitive OCT is evident for inspection of birefrigent tissues, such as muscles, cartilage, skin, coronary artery, outer ocular tissues, tissues of retina, and vocal cords. For soft biological tissues with weak birefringence (such as mucous and serous linings), polarization effects can also manifest themselves in OCT images. The modeling of polarization phenomena demonstrated that they can lead to the appearance of false layers in the images because of the influence of the above-mentioned modulation of the intensity due to the birefringence. Evidently, the appearance of such false layers is not acceptable in the interpretation of OCT images of layered structures [48]. Besides, because of the complexity of the near-surface structure of biological tissues, relatively simple algorithms that provide information on birefringence and orientation of optical axes can be developed only for the upper birefringent layer or for tissues with rather weak birefringence: the waves with orthogonal polarization should acquire a phase difference significantly smaller than 90° for all observation depths. Information about the direction of optical axes in deeper layers is distorted by birefringence in the upper layers [20, 48], so that retrieving this information requires more complex algorithms based on information above the upper layer [20, 48]. To single out the regions of biological tissues with different directions of optical axes, color encoding can be used [20].

Evidently, for the complex multifragment structure of soft biological tissues with weak birefringence, exact quantitative information on the directions of the optical axes and the degree of birefringence in various tissue fragments plays a secondary role, especially for medical screening and clinical applications. In this context, it looks attractive to apply the capabilities of cross-polarization OCT for qualitative differentiation of various fragments by their polarization characteristics, and differences between OCT images obtained in co- and cross-channels.

The above-mentioned approaches to obtaining polarization-sensitive images can be used as a basis for designing improved variants of endoscopic OCT devices with faster image acquisition and simultaneous real-time presentation of complementary images formed via co- and cross-polarization channels. In particular, the common-path fiber-optic scheme ensures stable images in the co-polarization channel without individual tuning of the optical arms in changeable endoscopic probes in the course of OCT inspection of tissues. However, sensitivity of the cross-polarization OCT in the optical schemes based on single-mode fibers depends on the polarization of the incident interrogating beam. Elimination of unstable sensitivity of the cross-polarization channel should allow for both qualitative and quantitative comparison between the co- and cross-polarization images obtained under given conditions. Improvement of the cross-polarization channel in OCT imaging is important not only for obtaining complementary polarization-sensitive and conventional intensity imaging, but also for extracting information on the directions of optical axes. Integrated solution of such problems is important for improving reliability of endoscopic OCT-based diagnostics and quality of evaluation of biological-tissue state in various clinical applications.

3. PROBLEM OF ELASTOGRAPHIC MAPPING IN OCT

Elastographic mapping [49] is another direction in the development of OCT aimed at obtaining additional information to complement the conventional intensity (structural) images. The term "elastography" in OCT is introduced by analogy with medical ultrasound and is usually understood as mapping of the spatial distribution of either shear elastic modulus G or the Young modulus E. It is well known that for most

part of biological tissues (except for bones and cartilage) the shear modulus G is much less than the bulk elastic modulus K, so that the Poisson's ratio ν is very close to 0.5, the value typical of liquids (notice that the exact equality $\nu = 1/2$ corresponds to zero shear modulus $G = 0$). As a result, for almost all biological tissues, the shear and Young moduli are proportional to each other with the same coefficient, since in the isotropic approximation $E = 2(1 + \nu)G \approx 3G$ [50]. In view of this, the literature on elastography quite often does not indicate which particular modulus (G or E) is mapped, and the term "stiffness" that has no rigorous definition is used. For a given value of the bulk modulus, higher values of the shear modulus characterize the ability of a soft tissue to maintain its shape. Just by this reason, the procedure of conventional palpation gives elastographic information: fingers feel an inclusion with a higher shear modulus as a stiffer region surrounded by easier deformable soft tissue.

For medical purposes the mapping of stiffness distribution in soft (i.e., other than cartilage or bone tissues) is important, because variability of the shear modulus (stiffness) is much higher compared with variability of the bulk modulus. Namely, the stiffness of the same soft tissue in normal and pathological states may differ several times and even orders of magnitude in contrast to rather weak (on the order of a few per cent) complementary variations of the bulk modulus. On the other hand, it is the bulk modulus which determines the impedance of ultrasound waves, and just its weak variations are visualized in conventional ultrasonic medical scanners. Thus, eventual variations in the shear modulus are not directly visualized either in conventional ultrasound echography, or in OCT images, because they characterize the scattering properties of the tissue with respect to longitudinal ultrasonic waves and transverse optical waves.

In view of this, to extract information on stiffness of the inspected tissue one has to perform additional image processing and compare conventional OCT images of a tissue subjected to either quasistatic or dynamic deformation. The latter approach can imply the excitation of either relatively low-frequency vibrations [51], or surface Rayleigh waves (e.g. induced by a miniature air-gun system [52]), or bulk shear waves (e.g., utilizing radiation pressure of focused ultrasonic beams [53]). Since the velocities of Rayleigh and shear waves are determined by the shear elastic modulus, measuring their velocities by OCT means allows for quantitative evaluation of the tissue stiffness. However, such methods require additional devices for excitation of vibrations or waves, so that here we focus on approaches that do not require additional technical means and thus are especially interesting for implementation in practical multimodal OCT devices.

In medical ultrasound, similar studies aimed at combining elastography with the capabilities of conventional ultrasonic scanners have been actively carried out over two decades [54]. As a result, in recent years several ultrasonic scanners with implemented capabilities of elastographic mapping have become commercially available [55]. This additional feature significantly increased the information content and improved specificity of ultrasonic diagnostics. In OCT, similar studies of the prospects for realization of elastographic mapping [49] started about one decade later than in ultrasound. In many aspects, such studies have been based on the elastographic approaches used in ultrasound. However, unlike the medical ultrasonic scanners, OCT scanners capable of elastographic mapping are not yet commercially available. This fact is related, in particular, to certain features of OCT images which complicate direct transfer of elastographic processing principles from the medical ultrasound to OCT, as is discussed in the following sections.

4. ELASTOGRAPHIC METHODS BASED ON THE INITIAL RECONSTRUCTION OF THE DISPLACEMENTS IN DEFORMED TISSUES

Detailed consideration of various elastographic approaches discussed in the literature is not the goal of the present paper which is primarily focused on the issue of creating a potentially practical multimodal OCT device. For such a scanner, different regimes should not require application of significantly different hardware features. In such a context, especially attractive for realization of elastographic mapping looks the possibility of utilization of the OCT probe itself for producing quasistatic deformation of the inspected tissue. Elastographic information in such a case should be extracted by appropriate processing of the OCT images of the deformed medium.

Conventionally in such a context it is assumed that at the first stage one should reconstruct the tissue

displacements produced by the OCT probe. Then the local strains should be determined by numerical differentiation of the reconstructed displacements [49]. Since in the probe vicinity the elastic stress is approximately uniform, the regions with increased stiffness better conserve their shape and, correspondingly, the local strains in such regions are smaller even if their translational displacements (that do not affect the relative mutual positions of the tissue constituents) are not small. The difference in the local strains found as a result of such a two-stage procedure gives information on the relative stiffness in different regions. It makes sense to call this group of approaches "displacement based" (DB-approaches), because at the initial stage they use the reconstruction of the displacements, although particular methods of the displacement-field reconstruction can significantly differ. Despite such differences, a significant part of elastography-related OCT studies starting from the first publications till present [49, 57–62] focuses on the DB-approaches (in a wide sense of this term).

4.1. Correlation approach to reconstruction of the displacement field

For determining displacements in different spatial regions, by analogy with medical ultrasonics, it seems natural to use cross-correlation between the compared OCT images (obtained at different compression levels) using a sliding correlation window. This procedure corresponds to maximization of the correlation coefficient $C_{x,z}(n,k)$:

$$C_{x,z}(n,k) = \frac{\sum\limits_{i=1}^{m_1}\sum\limits_{j=1}^{m_2}\left(S_{i,j}-\mu^S\right)\left(F_{i+n,j+k}-\mu^F_{n,k}\right)}{\left[\sum\limits_{i=1}^{m_1}\sum\limits_{j=1}^{m_2}\left(S_{i,j}-\mu^S\right)^2\sum\limits_{i=1}^{m_1}\sum\limits_{j=1}^{m_2}\left(F_{i+n,j+k}-\mu^F_{n,k}\right)^2\right]^{1/2}}, \tag{1}$$

where S is a fragment of the reference OCT image $m_1 \times m_2$ elements in size centered at the point $(x,\, z)$. The corresponding fragment F within a window of the same size is taken from the compared (strained) image. The position of the center of this window slides within a certain search region, which corresponds to searching for such parameters n and k in Eq. (1), for which the correlation coefficient $C_{x,z}$ reaches a maximum. The quantities μ^S and μ^F are the mean values found over the correlation windows S and F, respectively. For identical regions, correlation coefficient (1) reaches its maximum unity value at zero displacements $n = k = 0$. If the compared image represents deformed tissue, the sliding window is moved within a certain search area centered at $(x,\, z)$ at the reference image to find such coordinates n^* and k^* of the window F center, for which the best coincidence of the windows S and F is obtained and correlation coefficient (1) reaches a maximum. The so-found coordinates $(n^*,\, k^*)$ of the window F, for which the correlation coefficient reaches a maximum, define the displacement vector corresponding to the new position of the group of scatterers localized within the window S in the reference image.

Such a correlation approach for reconstructing the displacement field was discussed, in particular, in [49] and in later publications [57, 58]. Researches clearly understood that OCT images are characterized by a pronounced speckle structure [63–65]. In principle, such a speckle structure can be displaced as a whole if the scatterers do not experience mutual displacements relative to each other (for example, in the case of a pure translational displacement). However, in most cases of practically interest, the displaced areas experience deformations, which does cause mutual displacement of sub-resolution scatterers located within the sample volume with the axial size limited by the coherence length. For a sufficiently strong deformation, the speckle spots are not only displaced, but also may change their brightness, sometimes quite significantly. Thus, individual speckles in OCT images of deformed tissues exhibit pronounced "blinking" and peculiar "boiling" of the speckle pattern, which may completely destroy the cross-correlation between compared images at the speckle level.

In the context of the problem of decorrelation at the speckle level, note that if the tissue image has larger-scale features of morphological origin, which results in the appearance of the corresponding larger-scale components in the spatial spectrum, then spatio-temporal filtering of smaller-scale speckle blinking

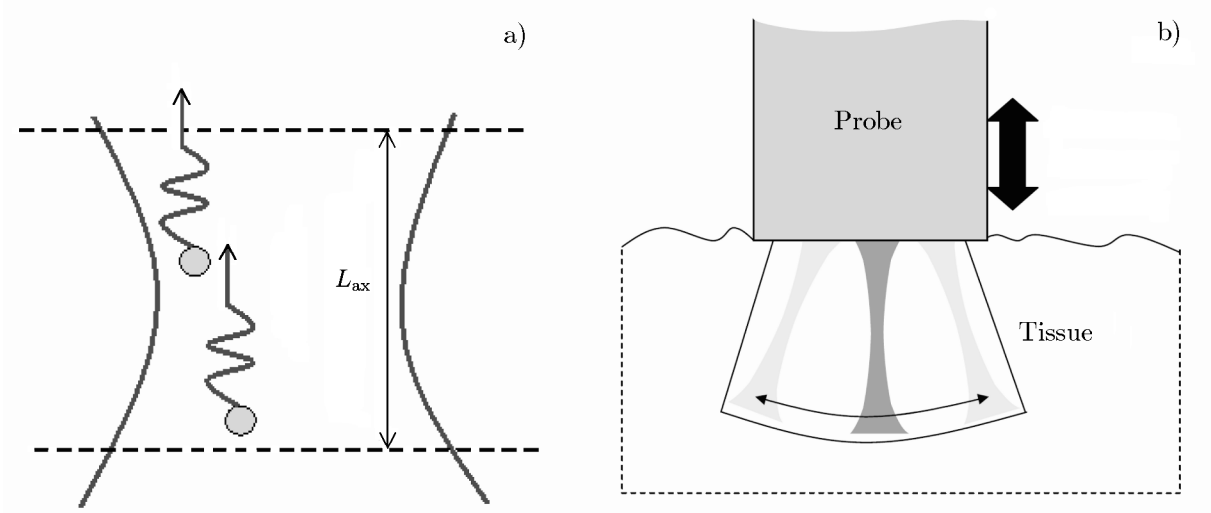

Fig. 2. Illustration of the sub-resolution scatterers localized within the sample volume and the backscattered optical waves with random mutual phasing dependent on the random separation of the scatterers (*a*). The interference of these waves results in the appearance of speckle patterns in OCT images, as well as speckle blinking if the tissue is deformed. Plot (*b*) shows the schematic of the tissue straining caused by the compression created by the rigid surface of the OCT probe (the direction of straining is shown by a vertical arrow).

can help to keep a quite noticeable correlation between compared images [66, 67].

However, such a procedure of retaining only larger-scale image features leads to a significant reduction in the resolution of the resultant field of cross-correlation in comparison with correlation at the smallest-scale speckle level. Besides, many tissues do not exhibit pronounced morphological features. In view of this, it is desirable to perform the correlation processing at the level of the speckle structure which is always present in OCT images. It is conventionally believed that for sufficiently small deformations, the effect of speckle blinking can be sufficiently weak, such that the correlation tracking of the speckle-spot displacements (and thus tissue displacements) should be possible. Following [49], the corresponding procedure is called speckle tracking.

Despite the apparent simplicity of the speckle-tracking idea, till now it has not resulted in practical and robust methods of the displacement-field reconstruction for elastographic applications in OCT. At the same time, it is well known that similar correlation procedures are successfully applied for reconstruction of displacement and strain fields in engineering problems, where digital photos of deformed samples are compared (the so-called methods of digital image correlation, DIC) [68–72]. In what follows we present some simple model arguments and estimates demonstrating that the difficulties of transferring these methods to speckle tracking in OCT are indeed significant. These arguments show that the satisfactory reconstruction of the displacements based on the speckle-level correlation procedures indeed can be achieved in OCT only under very special conditions.

Let us consider a simple model of speckle spot formation due to interference of a pair of optical waves scattered by two sub-resolution scatterers located within a sample volume of an OCT scanner (see Fig. 2). The result of interference of these waves is determined primarily by the axial separation of the scatterers, because they are usually located in the Fraunhofer zone of the receiving element, so that the phase difference due to the lateral separation within the scanning beam can be neglected (to first order). In view of this, the optical waves that first propagate to and then return from the pair of scatterers separated by the distance Δz in the axial direction acquire the phase difference $\Delta\varphi = 2k\,\Delta z$, where k is the wavenumber. The random separation Δz of the sub-resolution scatterers is smaller than the coherence length $L_{\rm ax}$ that determines the axial resolution of the OCT scanner. The resultant intensity $I_{\rm res}$ of the signal received from these scatterers is given by the expression

$$I_{\rm res} = I_1 + I_2 + 2\sqrt{I_1 I_2}\,\cos[\Delta\varphi], \tag{2}$$

where I_1 and I_2 are the intensities of each of the two backscattered components. For simplicity, in what follows we consider the identical intensities $I_1 = I_2 = I$.

If the tissue is strained with strain magnitude s, the modified phase difference is given by $\Delta\varphi(s) = 2k\,\Delta z\,(1+s)$. This expression takes into account the fact that it is the small difference Δz in the axial coordinates of the sub-resolution scatterers within the sample volume that dominates the phase difference $\Delta\varphi(s)$ of the interfering waves. Indeed, the other (although significantly greater) parts of the optical paths practically coincide and eventual inhomogeneities along those paths introduce the same variation in the phases of both interfering waves. Consequently, the deformation of the tissue causes a phase-difference variation given by the expression $\delta[\Delta\varphi(s)] = 2k\,\Delta z\,s$, in which only the initial difference Δz in the axial coordinates of the scatterers is present.

Evidently, intensity (2) is most sensitive to the small phase variation $\delta[\Delta\varphi(s)]$ in the vicinity of the steepest derivative of the phase factor $\cos[\Delta\varphi(s)]$, i.e., for $2k\,\Delta z = \pi/2 + \pi m$ (here m is an integer), corresponding to $\cos[\Delta\varphi(s)] = \pm\sin(2k\,\Delta z\,s) \approx \pm 2k\,\Delta z\,s$. It should be emphasized that the discussed condition of strong sensitivity of the phase factor is not a significant limitation, because the derivative of a sine function $\sin(x)$ varies fairly slowly with increasing argument x in the range from 0° to 90°. For example, even for $x = 60°$, the derivative decreases only by a factor of two. Thus, it can be said that the above-mentioned condition of the high strain sensitivity of the phase factor concerns approximately $60/90 \approx 70\,\%$ of all speckles in an OCT image.

In view of these arguments, Eq. (2) indicates that the strain s causes a variation in the intensity of the most part of speckle spots by

$$\delta I_{\text{blink}}(s = d/H) \approx 4I_0 k\,\Delta z\,s. \tag{3}$$

In Eq. (3), the strain $s \approx d/H$ is approximately (neglecting tissue the inhomogeneity) related to the axial displacement d of the considered scattering volume and its depth H counted from the rigid surface of the probe that produces deformation of the tissue. We emphasize that the intensity variation δI_{blink} (speckle blinking) given by Eq. (3) has no relation to the displacement of the speckle spot as a whole, and is entirely due to the tensile or compressional straining of the tissue.

On the other hand, the same strain s that causes a variation in the size of the scattering volume (responsible for speckle blinking) also causes a displacement of the entire scattering volume, which results in the intensity variation in the vicinity of the initial position of the speckle spot. The latter variation is of purely geometric origin and is due to the displacement of the entire speckle. To evaluate the magnitude of the intensity variation due to a geometric displacement of the speckles we, as above, limit ourselves to considering the displacements along the z coordinate. Let $I(z)$ be the initial distribution of the intensity in the OCT image. Then for the speckle corresponding to the scattering volume with the depth $z = H$, the displacement of the scatterers by the distance d causes a variation in the intensity of the considered speckle by

$$\delta I_{\text{geom}}(d) \approx d \cdot \partial I(z)/\partial z \approx d \cdot I_0/(D/2) = 2I_0 H s/D, \tag{4}$$

where D is the characteristic diameter of one intensity spot. Equation (4) shows that, in contrast to the intensity variation δI_{blink} that is determined only by the local strain s, the variation δI_{geom} is determined by the displacement d of the scattering volume and consequently for a given strain s, also depends on the depth H.

The aim of speckle tracking is the detection of displacements of the scattering volumes. Those displacements determine exclusively the variations δI_{geom} in contrast to the variations δI_{blink} (speckle blinking) related to changes of mutual positions of the sub-resolution scatterers within each sample volume. This means that the realization of speckle tracking requires that the geometric intensity variations $\delta I_{\text{geom}}(d)$ strongly dominate over the variations δI_{blink} related to the speckle blinking:

$$\delta I_{\text{geom}}/\delta I_{\text{blink}} \gg 1. \tag{5}$$

For example, let us require that the correction to the variation in the intensity of the speckle spot related

to blinking does not exceed 20 % (that is $\delta I_{\rm geom}/\delta I_{\rm blink} \geq 5$). Let us also recall that the phase difference between the waves from the sub-resolution scatterers is $2k\,\Delta z = 4\pi\,\Delta z/\lambda$ (where λ is the optical wave length), and for random location of the scatterers within the sample volume, the characteristic distance between such sub-resolution scatterers can be estimated as $\Delta z \approx L_{\rm ax}/2$.

Then Eqs. (3) through (5) yield the following condition on the minimun depth for the scattering volume:

$$H \geq 10\pi D L_{\rm ax}/\lambda. \tag{6}$$

Next, let us take into account that the minimum size D of a speckle spot in a pixelized image should not be less than two pixels in order to satisfy the Nyquist-Kotelnikov criterion, and also use in the estimate a typical OCT system coherence length $L_{\rm ax} \approx 10\lambda$. Then the inequality (6) yields the following estimate of the minimum depth (in pixels) required for fairly reliable speckle tracking:

$$H \geq 200\pi \approx 628 \text{ (pixels)}. \tag{7}$$

The obtained estimate shows that for typical parameters of OCT systems, implementation of reliable speckle tracking is problematic and may in fact be impossible for significant parts of an OCT image. Numerical examples [73, 74] confirm that actual displacements of the scatterers can be strongly masked by speckle blinking. Those examples also show that even at the initial stage of deforming the tissue, the speckle blinking can mask not only axial, but also lateral displacements. This is due to the fact that lateral deformation of the compressed tissue is accompanied by axial straining. This axial straining in turn causes the masking decorrelation due to speckle blinking, despite the fact that the lateral mutual displacements of the sub-resolution scatterers do not directly contribute to significant speckle blinking.

Usually, discussions of speckle tracking have been conducted under the assumption that for sufficiently small strains that do not yet cause significant variations in the intensity of speckles, the tracking of speckle displacements by correlation processing can be guaranteed. However, the above-presented arguments show that it is the properties of the OCT system (first of all, the optical wavelength and the coherence length) which determines the degree of masking of the actual displacements by the influence of speckle blinking, and the degree of this masking can be significant even for very small strains, which at first glance looks counter-intuitive. In this context, it becomes clear why for modern ultrasound scanners, for which the length of the sound pulse (the counterpart of $L_{\rm ax}$ in OCT) can approach one wavelength, the limitations related to the influence of speckle blinking are much less severe. This explains why in reconstruction of strain fields in OCT the speckle tracking is not as efficient as in a similar processing of images given by ultrasonic scanners. Generally speaking, the speckle structure of images discussed above for OCT systems with $L_{\rm ax}/\lambda \approx 10$ should be present in the images obtained even by systems with $L_{\rm ax}/\lambda \approx 1$, for a super-broadband OCT system described in [63] or modern ultrasonic scanners. However, the masking influence of speckle blinking in the latter case should be much weaker. Similarly, in the absence of speckle blinking, the correlation approach to reconstruction of displacements (digital image correlation) works very well in engineering applications based on the processing of photographic images of deformed samples [68–72].

4.2. Reconstruction of displacements based on phase measurements

In view of the above discussed difficulties in realization of correlation methods for reconstruction of displacement fields in OCT, it is not surprising that in recent years ever increasing attention has been paid to the feasibility of displacement measurements based on phase methods [59–61, 75]. Some of those works demonstrate significantly better possibilities for the phase approach to displacement-field reconstruction, compared with the correlation methods (e.g., [75]). In such methods, first of all, axial displacements are discussed. Formally, in the phase methods of displacement measurement, the variation in the mutual distance between the sub-resolution scatterers also contributes to the phase variation for the received signal. However, this contribution produces much weaker masking effect compared to the speckle-intensity blinking

in the correlation-based speckle tracking.

Let us compare the role of the mutual displacements for a pair of sub-resolution scatterers in the case of phase measurements and in the above-considered correlation speckle tracking assuming the same parameters of the OCT scanner. The resultant signal produced by a pair of scatterers localized within a sample volume is formed by the corresponding pair of waves that can be conveniently written in the complex-valued form assuming for simplicity identical strength of the scatterers:

$$a_1 = A\exp[i\,2k\,(H - \Delta z/2)\,(s+1)]; \tag{8a}$$

$$a_2 = A\exp[i\,2k\,(H + \Delta z/2)\,(s+1)]. \tag{8b}$$

Here, as before, s is the axial strain of the tissue, H is the depth of the center of the sample volume, and the maximum axial distance between the sub-resolution scatterers is limited by the axial coherence length, $\Delta z \le L_{\rm ax}$. The resultant field $a = a_1 + a_2$ takes the form

$$a = 2\tilde{A}\cos[k\,\Delta z\,(s+1)]\exp(2ikHs). \tag{9}$$

Here, the complex amplitude $\tilde{A} = A\exp(2ikH)$ is introduced that does not depend on the strain s. The last phase factor in Eq. (9) describes the variation of phase for the wave backscattered from the sample volume with the center at $z = H$. The factor $\cos[k\,\Delta z\,(s+1)]$ is due to interference of the fields from the two subresolution scatterers and describes the dependence of intensity of the resultant speckle spot on the initial axial separation Δz of the scatterers and the strain s.

The received wave interferes with the reference field at the photo-receiver, which transforms the variation of the wave phase into variations in the intensity $I_{\rm d}$ at the phase detector. The intensity $I_{\rm d}$ can be found by analogy with Eq. (2), where the intensities I_1 and I_2 are changed to the intensity $I_{\rm a}$ of the received wave given by Eq. (9) and the reference-wave intensity $I_{\rm r}$:

$$I_{\rm d} = I_{\rm r} + I_{\rm a} + 2\sqrt{I_{\rm r}I_{\rm a}}\,\cos[\Delta\varphi(s)]. \tag{10}$$

Here, the quantity $\Delta\varphi(s) = 2kHs - \varphi_{\rm r}$ has the meaning of the difference between the phase $\varphi_{\rm r}$ of the reference wave and the phase $2kHs$ of the received sample wave [Eq. (9)]. The appropriate choice of the reference phase ensures the maximum sensitivity of the factor $\cos[\Delta\varphi(s)]$ in Eq. (10) to the small phase variations $2kHs < 1$. In such a case, the displacement $d = Hs$ yields intensity variation by

$$|\delta I_{\rm d}(Hs)| = 4I_0kHs, \tag{11}$$

where for simplicity it is assumed that $I_{\rm a}(s=0) = I_{\rm r} = I_0$.

In principle, the intensity $I_{\rm d}$ given by Eq. (10) can also experience variations due to a variation in the intensity $I_{\rm a}$ (including the variation in the speckle-spot intensity due to speckle blinking). The latter, as is seen from Eq. (9), relates to the variations in the distance between the sub-resolution scatterers in the strained tissue, $I_{\rm a} = |a|^2 = 2A^2\,\{1 + \cos[2k\,\Delta z\,(s+1)]\}$. By analogy with the discussion of Eq. (2), one can conclude that the strongest variations in $I_{\rm a}$ should be observed at $2k\,\Delta z = \pi/2 + \pi m$, i.e., for $\cos[2k\,\Delta z\,(s+1)] = \pm\sin(2k\,\Delta z s) \approx \pm 2k\,\Delta z\,s$. Since the separation Δz of the scatterers does not exceed $L_{\rm ax}$, the maximum value of those blinking-related variations is of the order of $\delta I_{\rm a} \approx 2I_0k\,\Delta z\,s \le 2I_0kL_{\rm ax}s$. Comparison of the latter expression with Eq. (11) indicates that for the discussed small deformations and under the condition $H \gg L_{\rm ax}$ (valid for the most part of the image), speckle blinking yields only negligible corrections to the displacements based of the phase measurements. Thus, there is a strong difference from the above-considered case of correlation approach to reconstruction of displacements, because for the latter, under the usually valid condition $L_{\rm ax}/\lambda \gg 1$, the speckle blinking can produce very strong masking effect over a significant part of the image. This masking effect does not disappear even for very small strains. In contrast, the above-presented arguments demonstrate that in the phase method the blinking-induced error on the order $L_{\rm ax}/H$ in the estimate of actual phase variations is negligible (except for the minimal

depths $H \approx L_{\text{ax}}$), so that for small strains $s < 1/(2kH)$, this measurement error is not important for correct estimation of the displacement almost everywhere over an OCT image.

Therefore, modern technical means that routinely ensure the accuracy of phase measurements of the order of a degree make it possible to measure displacements $d \ll \lambda$ in OCT. Since $\lambda \ll H$, it can be said that the eventual uncertainty proportional to an integer number of wavelengths in the phase method does not occur for sufficiently small strains, $Hs \ll \lambda < L_{\text{ax}}$, i.e., exactly for the discussed small sub-pixel displacements over the entire area of an OCT scan.

At the next stage, for evaluating local stiffness of the tissue, one needs to reconstruct local strains, for which numerical differentiation of the earlier reconstructed displacement field is required. This differentiation actually estimates the local value of the ratio

$$s(z) \approx (d_2 - d_1)/(z_2 - z_1), \tag{12}$$

where z_1 and z_2 are the initial positions of the scatterers displaced by the distances d_1 and d_2, respectively. Therefore, the quality of the differentiation is determined by the inaccuracy of measuring both the scatterer displacements d_1 and d_2 and their initial positions z_1 and z_2. Although the displacements d_1 and d_2 can be measured with a fairly high sub-pixel accuracy (e.g., using phase methods as argued above), the distances z_1 and z_2 in the best case are known with accuracy determined by the vertical resolution L_{ax}. The latter in the pixelized OCT image cannot be better than 1-2 pixels (when the minimal requirements of the Nyquist-Kotelnikov criterion are satisfied). Besides, inhomogeneities of the refraction index in real tissues can introduce additional errors in the estimation of the distances z_1 and z_2. In some works (for example, [59,60]) instead of the estimate (12) of the genuine local strain, the authors suggested using the quantity

$$\varepsilon(z) = d(z)/z, \tag{13}$$

also called depth-dependent strain. However, the quantity $\varepsilon(z)$ characterizes merely the average strain of the entire layer with the thickness z. Certainly, the so-defined strain is more robust with respect to the measurement errors compared with genuine local strains, but it has no direct relation to the local tissue parameters and does not directly show differences in the local stiffness.

Similar problems of numerical differentiation arise in the correlation methods of the displacement-filed reconstruction based on speckle tracking. As argued above, for typical parameters of many OCT scanners, the errors in the reconstruction of displacement d due to the speckle blinking can be significantly higher than for phase measurements. Furthermore, for some parameters of OCT scanners, the correlation speckle tracking can be impossible over almost the entire area of OCT scans. In such a context, despite the remaining difficulties in performing the error-sensitive numerical differentiation, the phase method has significant advantages in comparison with the correlation speckle tracking from the viewpoint of accuracy and robustness with respect to the influence of speckle blinking.

In view of the above-mentioned problem of numerical differentiation of displacements reconstructed by one or another method, it seems interesting to find a possibility to completely exclude the necessity of the numerical differentiation either via estimation of ratio (12) or using equivalent processing procedures. In such a context, another variant of utilization of correlation procedures yields attractive prospects. This approach is not based on the initial reconstruction of displacements, but directly uses the degree of decorrelation between images for obtaining information on the local stiffness of the tissue. This recently proposed approach to the elastographic mapping in OCT [73, 74], as well as methods of visualizing the vasculature (blood circulation), in which a somewhat similar usage of decorrelation can be successfully applied, will be discussed in the second part of this paper.

This work was supported by the Russian Foundation for Basic Research (project Nos. 12–02–01160, 13–02–00627, and 13–02–97131) and the Russian Federation Government (contracts 11.G34.31.0066 and 14.B25.31.0015). L.A.M. acknowledges the support of the grant of the Russian Federation president for young researchers (grant MK-4826.2013.2).

REFERENCES

1. D. Huang, E. A. Swanson, C. P. Lin, et al., *Science*, **254**, 1178 (1991).
2. E.A. Swanson, J. A. Izatt, M. R. Hee, et al., *Opt. Lett.*, **18**, No. 21, 1864. (1993).
3. Y. T. Pan, T. Q. Xie, C. W. Du, et al., *Opt. Lett.*, **28**, No. 24, 2485. (2003).
4. M. C. Skala, A. Fontanella, H. Hendargo, et al., *Opt. Lett.*, **34**, No. 3, 289. (2009).
5. G. V. Gelikonov, V. M. Gelikonov, F. I. Feldchtein, et al., *Conference on Laser and Electro-Optics (Washington, USA)*, Optical Society of America, Baltimore, 210 (1997).
6. F. I. Feldchtein, G. V. Gelikonov, V. M. Gelikonov, et al., *Opt. Express*, **3**, No. 6, 239 (1998).
7. Y. Pan and D. L. Farkas, *J. Biomed. Opt.*, **3**, No. 4, 446 (1998).
8. J. M. Schmitt and S. H. Xiang, *Opt. Lett.*, **23**, No. 13, 1060 (1998).
9. *Optical Coherence Tomography: Techology and Applications*, Ed. by J. G. Fujimoto and W. Drexler. Springer, Berlin (2008).
10. M. R. Hee, D. Huang, E. A. Swanson, et al., *J. Opt. Soc. Am.* , **9**, 903 (1992).
11. P. 934. J. F. De Boer, T. E. Milner, M. J. C. Van Gemert, et al., *Opt. Lett.* **22**, No. 12, 934 (1997).
12. J. F. De Boer, S. M. Srinivas, A. Malekafzali, et al., *Opt. Express*, **3**, No. 6, 212 (1998).
13. M. J. Everett, K. Schoenenberger, B. W. Colston Jr., et al., *Opt. Lett.*, **23**, No. 3, 228 (1998).
14. M. C. Booth, G. Di Giuseppe, B. E. A. Saleh, et al., *Phys. Rev. A*, **69**, No. 4. 043815 (2004).
15. B. Liu, M. Harman, S. Giattina, et al., *Appl. Opt.*, **45**, No. 18, 4464 (2006).
16. K. H. Kim, B. H. Park, Y. Tu, et al., *Opt. Express*, **19**, No. 2, 552 (2011).
17. R. V. Kuranov, V. V. Sapozhnikova, I. V. Turchin, et al., *Opt. Express*, **10**, No. 15, 707 (2002).
18. J. F. De Boer, T. E. Milner, and J. S. Nelson, *Opt. Lett.*, **24**, No. 5, 300 (1999).
19. G. Yao and L. V. Wang, *Opt. Lett.*, **24**, No. 8, 537 (1999).
20. C. K. Hitzenberger, E. Gotzinger, M. Sticker, et al., *Opt. Express*, **9**, No. 13, 780 (2001).
21. N. Ghosh and I. A.Vitkin, *J. Biomed. Opt.*, **16**, No. 11, 110801 (2011).
22. D. Fried, J. Xie, S. Shafi, et al., *J. Biomed. Opt.*, **7**, No. 4 618 (2002).
23. V. Sankaran, J. T. Walsh, D. J. Maitland, *J. Biomed. Opt.*, **7**, No. 3, 300 (2002).
24. R. V. Kuranov, V. V. Sapozhnikova, N. M. Shakhova, et al., *Quantum Electron.*, **32**, No. 11, 993 (2002).
25. N. Gladkova, O. Streltsova, E. Zagaynova, et al., *J. Biophoton.*, **4**, Nos. 7–8, 519 (2011).
26. J. F. De Boer, S. M. Srinivas, B. H. Park, et al., *IEEE J. Sel. Top. Quantum Electron.*, **5**, No. 4, 1200 (1999).
27. M. C. Pierce, B. H. Park, B. Cense, et al., *Opt. Lett.*, **27**, No. 17, 1534 (2002).
28. W. Y. Oh, B. J. Vakoc, S. H. Yun, et al., *Opt. Lett.*, **33**, No. 12, 1330 (2008).
29. W. Y. Oh, S. H. Yun, B. J. Vakoc, et al., *Opt. Express.*, **16**, No. 2, 1096 (2008).
30. V. M. Gelikonov and G. V. Gelikonov, *Laser Phys. Lett.*, **3**, No. 9, 445 (2006).
31. V. M. Gelikonov and G. V. Gelikonov, *Quant. Electron.*, **38**, No. 7, 634 (2008).
32. S. L. Jiao, W. R. Yu, G. Stoica, et al., *Opt. Lett.*, **28**, No. 14, 1206 (2003).
33. V. P. Tishkovets and M. I. Mishchenko, *J. Quant. Spec. Rad. Transfer.*, **110**, No. 1–2, 139 (2009).
34. J. F. De Boer and T. E. Milner, *J. Biomed. Opt.*, **7**, No. 3, 359 (2002).

35. J. E. Roth, J. A. Kozak, S. Yazdanfar, et al., *Opt. Lett.*, **26**, No. 14, 1069 (2001).
36. B. Cense, T. C. Chen, B. H. Park, et al., *Opt. Lett.*, **27**, No. 18, 1610 (2002).
37. D. P. Dave, T. Akkin, and T. E. Milner, *Opt. Lett.*, **28**, No. 19, 1775 (2003).
38. J. Zhang, S. Guo, W. Q. Jung, et al., *Opt. Express*, **11**, No. 24, 3262 (2003).
39. T. Yoshino, T. Hashimoto, M. Nara, et al., *J. Lightwave Technology*, **10**, No. 4, 503 (1992).
40. J. Bush, F. Feldchtein, G. Gelikonov, et al., *SPIE Proc. 17th Int. Conf. Opt. Fibre Sensors*, **5855**, 254 (2005).
41. F. I. Feldchtein, J. Bush, G. V. Gelikonov, et al., *SPIE Proc. Coherence Domain Optical Methods and Optical Coherence Tomography in Biomedicine IX*, **5690**, 349 (2005).
42. U. Sharma, N. M. Fried, and J. U. Kang, *IEEE J. Sel. Top. Quantum Electron.*, **11**, No. 4, 799 (2005).
43. Patent No. 6847453 US. All fiber antocorrelator / I. J. Bush (2005).
44. A. D. Drake and D. C. Leiner, *Rev. Sci. Instrum.*, **55**, No. 2, 162 (1984).
45. J. Bush, P. Davis, and M. A. Marcus, *SPIE Proc. Fiber Optic Sensor Technology II*, **4204**, 71 (2001)
46. Authorship certif. No. 1315797 A1 SSSR, *Optical fiber sensor* [in Russian], V M. Gelikonov, V. I. Leonov, and M. A. Novikov, Priorty of 04.05.1984; Published 07.06.1987, Bullet. 21, p.3.
47. V M. Gelikonov, D. D. Gusovskiy, V. I. Leonov, et al., *Pis'ma v Zhurn. Tekhn. Fiz.* [in Russian] **13**, No. 13, 775 (1987).
48. B. Liu, M. Harman, and M. E. Brezinski, *J. Opt. Soc. Am. A.*, **22**, No. 2, 262 (2005).
49. J. Schmitt, *Opt. Express*, **3**, No. 6, 199 (1998).
50. L. D. Landau and E. M. Lifshitz, *Theory of Elasticity*, Elsevier, Amsterdam (1986).
51. S. G. A. Adie, B. F. Kennedy, J. J. Armstrong, et al., *Phys. Med. Biology*, **54**, No. 10, 3129 (2009).
52. S. Wang, K. V. Larin, J. Li, et al., *Laser Phys. Lett.*, **10**, No. 7, 075605 (2013).
53. X. Liang, M.Orescanin, K. S. Toohey, et al., *Opt. Lett.*, **34**, No. 19, 2894 (2009).
54. J. Ophir, I. Cespedes, H. Ponnekanti, et al., *Ultrasonic Imaging*, **13**, 111 (1991).
55. K. J. Parker, M. M. Doyley, and D. J Rubens, *Phys. Med. Biology*, **56**, No. 1, R1 (2011).
56. J. M. Schmitt, S. H. Xiang, K. M. Yung, *J. Biomed. Opt.*, **4**, No. 1, 95 (1999).
57. C. Sun, B. Standish, and V. X. D. Yang, *J. Biomed. Opt.*, **16**, No. 4, 043001 (2001).
58. J. Rogowska, N. A. Patel, J. G. Fujimoto, et al., *Heart*, **90**, No. 5, 556 (2004).
59. J. Rogowska, N. Patel, S. Plummer, et al., *British J. Radiol.*, **79**, No. 945, 707 (2006).
60. S. J. Kirkpatrick, R. K. Wang, and D. D. Duncan, *Opt. Express*, **14**, No. 24, 11585 (2006).
61. R. K. Wang, S. Kirkpatrick, and M. Hinds, *Appl. Phys. Lett.*, **90**, No. 16, Art. no. 164105 (2007).
62. B. F. Kennedy, X. Liang, S. G. Adie, et al., *Opt. Express*, **19**, No. 7, 6623 (2011).
63. A. Nahas, M. Bauer, S. Roux, et al., *Biomed. Opt. Express*, **4**, No. 10, 2138 (2013).
64. T. R. Hillman, S. G. Adie, V. Seemann, et al., *Opt. Lett.*, **31**, No. 2, 190 (2006).
65. A. Curatolo, B. F. Kennedy, D. D. Sampson, et al., *Advanced Biophotonics: Tissue Optical Sectioning*, Ed. by V. Tuchin and R. K. Wang, Taylor and Francis, (2013), p. 183.
66. V. Y. Zaitsev, L. A. Matveev, A. L. Matveev, et al., *SPIE Proc.*, **8802**, 880208 (2013).
67. V. Y. Zaitsev, L. A. Matveev, G. V. Gelikonov, et al., *Laser Phys. Lett.*, **10**, No. 6, 065601 (2013).
68. M. A. Sutton, W. J. Wolters, W. H. Peters, et al., *Image Vision Computing*, **1**, No. 3, 133 (1983).

69. T. C. Chu, W. F. Ranson, and M. A. Sutton, *Experimental Mechanics*, **25**, No. 3, 232 (1985).
70. F. Hild, S. Roux, *Strain*, **42**, No. 2, 69 (2006).
71. B. Pan, K. Qian, H. Xie, et al., *Measurement Sci. Technol.*, **20**, No. 6, 062001 (2009).
72. B. Pan, *Experimental Mechanics*, **51**, No. 7, 1223 (2011).
73. V. Y. Zaitsev, L. A. Matveev, A. L. Matveyev, et al., *SPIE Proc. Optical Coherence Tomography and Coherence Techniques VI*, **8802**, 880208 (2013).
74. V. Y. Zaitsev, L. A. Matveev, A. L. Matveyev, et al., *J. Biomed. Opt.*, **19**, No. 2, 021107 (2014).
75. B. F. Kennedy, S. H. Koh, R. A. McLaughlin, et al., *Biomed. Opt. Express*, **3**, No. 8, 1865 (2012).